

The 2 μm spectrum of the auroral emission in the polar regions of Jupiter

L. Kedziora-Chudczer^a, D. V. Cotton^a, D. J. Kedziora^b, J. Bailey^a

^a*School of Physics, UNSW, 2052, Sydney, NSW Australia*

^b*School of Physics, The University of Sydney, 2006, Sydney, NSW Australia*

Abstract

We report observations of the high ($R \sim 18000$) and medium ($R \sim 5900$) resolution, near-infrared spectra of Jupiter's polar regions with the GNIRS instrument at the Gemini North telescope. The observations correspond to the area of main auroral oval in the South and the main spot of the Io footprint in the North. We detected and assigned 18 emission lines of the H_3^+ , $2\nu_2 \rightarrow 0$ overtone band in the region from 4800 to 4980 cm^{-1} and 5 additional lines in the extended low-resolution spectrum. We use our new modelling scheme, ATMOF to remove telluric absorption bands of CO_2 that feature strongly in the 2 μm region. The H_2 1-0 S(1), S(2) and S(3) emission lines are also detected in the observed spectral region. We found the rotational temperature and column density of H_3^+ emission at the peak intensity for both northern and southern auroral regions to be the same within the measurement errors ($T_{rot} \sim 950\text{K}$ and $N(\text{H}_3^+) \sim 4.5 \times 10^{16} \text{ m}^{-2}$). The estimates of T_{rot} from H_2 are consistent within much higher uncertainties with temperatures derived from H_3^+ emissions. We derived the profiles of the H_3^+ emissivity and ion density for both auroral regions providing the first such measurement for the emission associated with the main spot of the Io footprint. We also found a number of weaker lines in the high-resolution spectra that could be associated with emission from high excitation levels in neutral iron, which could be deposited in Jupiter's atmosphere as a result of meteor ablation.

Keywords: Infrared observations; atmospheres – structure, composition: Jupiter

Email address: lkedzior@unsw.edu.au (L. Kedziora-Chudczer)

1. Introduction

Jupiter's auroral emissions were first observed in the ultraviolet by Voyager 1 in 1979. Since then the Jovian aurora has been detected from space in X-rays by the ROSAT mission, in far UV by the IUE satellite, in visible by the Galileo spacecraft's SSI camera and from the ground at infrared and radio wavelengths (Bhardwaj & Gladstone, 2000). In the powerful magnetosphere of Jupiter the accelerating electrons and ions spiral down towards the polar regions while colliding with particles of the planetary atmosphere. The auroral display in the atmosphere of Jupiter and other giant planets arises due to excitation of hydrogen species rather than oxygen and nitrogen that give the characteristic colours of the aurora in the Earth's atmosphere. While the solar wind is thought to affect auroral emission on Jupiter the interaction of the moons, Io and Ganymede with Jupiter's magnetosphere contributes most ionised particles that form the magnetised plasma torus around the planet.

The observed auroral emissions are dominated by excitation, ionisation and dissociation processes that are due to energetic electrons impacting on hydrogen molecules. Heavier ions have also been observed in Jupiter's magnetosphere and are thought to contribute to the aurora. Volcanic activity on Io was proposed as the origin of these particles that are swept up and ionised in the planetary magnetosphere (Thorne & Tsurutani, 1979). The de-excitation of hydrogen and its molecular form, H_2 leads to the UV emission that appears to have a persistent presence in the polar regions of the planet (Grodent et al., 2003). Its most stable component is a characteristic, intense main oval emission, which forms due to the co-rotation breakdown of the plasma escaping radially from the torus. The Alfvénic currents generated at Io and other Galilean moons form arcs with bright spots of auroral emission in the vicinity of the main oval. These, so called footprints, change longitudinal position due to orbital motion of the moons within the magnetosphere co-rotating with the planet (Bonfond et al., 2013). The irregular in shape, highly variable, polar emissions are also visible inside the main oval.

On the other hand the ionized H_2 combines with a molecular neutral hydrogen in exothermic reactions leading to formation of the H_3^+ molecule responsible for auroral emission in the infrared. Observations of Jupiter in the far infrared also revealed strong limb brightening at high latitudes that was identified as emission due to bands of methane at $7.7 \mu\text{m}$, acetylene at $13.6 \mu\text{m}$, ethane at $12.2 \mu\text{m}$ and other hydrocarbons (Kim et al., 1985).

The H_3^+ molecule was first identified in laboratory plasmas produced in

discharge cells from H_2 gas (Thompson, 1911). It is the most abundant product of hot environments dominated by hydrogen. Therefore it is important in astrophysical plasmas such as planetary ionospheres and parts of the interstellar medium as a cooling agent during stellar formation (Adamowicz & Pavanello, 2012). H_3^+ is the simplest highly symmetric, triatomic molecule that makes theoretical *ab initio* calculations feasible. Such models show a good agreement with experimental spectra from laboratories and astronomical objects. The rotational spectrum of the molecule arises due to centrifugal distortion that leads to a small dipole moment. Such a “forbidden” spectrum has reasonably strong transitions due to the small nuclear mass of H_3^+ . Its vibrational spectrum with two modes ν_1 and ν_2 , leads to a complex structure of transitions in fundamental, overtone, forbidden and combination bands. The fundamental band, $\nu_2 \rightarrow 0$, located in the infrared region centred on 2521 cm^{-1} produces the strongest transitions. Although typical overtone transitions tend to be very weak in comparison, the H_3^+ molecule has much stronger first overtone $2\nu_2 \rightarrow 0$, transitions due to small masses and its largely anharmonic potential (Oka, 1992).

Both fundamental and overtone bands have been observed in Jupiter’s ionosphere. Many auroral emission features of H_3^+ were first detected in low-resolution spectra at $2 \mu\text{m}$ by Trafton et al. (1989) who were only able to identify H_2 S(1) and S(0) quadrupole lines. An assignment of other features followed from the work of Drossart et al. (1989), who observed Jupiter with the Fourier Transform Spectrometer (FTS) at the Canada-France-Hawaii Telescope between 2.0 and $2.2 \mu\text{m}$, and assigned 23 lines to the H_3^+ molecule in the $2\nu_2$ overtone band. This discovery prompted observations of the predicted to be stronger, fundamental ν_2 band of H_3^+ at $3.5\text{--}4 \mu\text{m}$ (Drossart et al., 1993; Maillard et al., 1990; Oka & Geballe, 1990). Transitions observed in both bands are useful probes of the physical conditions in the upper atmosphere of Jupiter. Measurements of temperatures, column densities and ortho-to-para ratios were followed by temporal monitoring and spatially resolved mapping of auroral regions (Miller et al., 1997; Stallard et al., 2002; Raynaud et al., 2004).

In this paper we present GNIRS/Gemini spectroscopic observations from the Jovian auroral regions (Section 2). We describe the application of the ATMOF modelling technique that allows effective removal of telluric absorption that is important in detecting weak spectral features (Section 3). In Section 4 we identify emissions from H_3^+ and H_2 and propose assignments for the remaining lines. Next we determine the rotational temperature, column

Table 1: Observing conditions and settings of the GNIRS instrument

Date UT	Jupiter CML III	Central wavelength	Resolution	Integration time	Mean airmass	Seeing
	<i>deg</i>	<i>μm</i>		<i>sec</i>		<i>arcsec</i>
24/08/2011 15:09	300	2.08	5900	60	1.01	0.4
27/08/2011 15:01	31	2.04	18000	160	1.009	0.25

density and vertical profiles of H_3^+ in the ionospheric region of the planetary atmosphere together with estimates of its maximum density (Section 5 and 6). We also use H_2 quadrupole lines detected in the low-resolution spectrum of the northern auroral region to derive rotational temperature for this molecule (Section 7). Finally we discuss and compare our measurements with previously published observations in Sections 8 and 9.

2. Observations and Data

We carried out high-resolution, long slit spectroscopy of the Jovian central meridian in the K band between 2.01 and 2.07 μm with the GNIRS instrument on the GEMINI North 8m telescope in August, 2011 (Table 1) as a part of the project to understand the D/H ratio in giant planets and Titan (Kedziora-Chudczer et al., 2013; Cotton et al., 2015).

The 0.1-arcsecond-wide slit positioned across the diameter of the planet in a direction encompassing the northern and southern polar regions, is marked as the yellow line in Figure 1. The slit was tilted at close to 22 degrees with respect to the planet’s rotation axis, which was a requirement of the main project but it proved less convenient for observations of auroral emissions. In the northern polar region (Figure 1 and 3) the slit was only grazing the outer edges of the typical extent of the UV aurora encompassing the Io footprint as defined in Grodent et al. (2003). In Figure 3 the expected position of the main Io footprint spot (Bonfond et al., 2009) is marked with the square on both northern and southern aurora. The size of both squares corresponds to measurement errors given in that paper. Interestingly, our northern spectrum falls onto the region, which encompasses the expected auroral emission from the main Io spot. In the south the slit cuts through the inner aurora, which should include the emissions associated with the main oval.

We used the 111 lines/mm grating to obtain a spectral resolution of $R \sim 18000$. These observations were complemented with lower-resolution spectra taken with the 32 lines/mm grating ($R \sim 5900$) to cover a broader

wavelength region in the K band centred on $2.08 \mu\text{m}$ between 1.96 and $2.17 \mu\text{m}$. We applied standard calibration techniques for the 2-D spectral images by using the Gemini IRAF GNIRS package. The images were aligned and the instrument specific noise due to variable bias was removed. Next the non-linearity correction was performed and the bad pixels on the detector frames were flagged. After that, images were flat-fielded and wavelength calibrated with Ar/Xe lamps. Finally the frames were sky-subtracted and the s-distortion correction was applied.

The auroral emission lines were clearly visible in the 2-D high-resolution spectra in both polar regions (see Figure 2 that shows the northern and southern spectral region with strong emission lines from H_3^+ at the edge of the limb of the planet). We extracted 1-D spectra for all spatial rows with visible auroral emissions. The pixel size of $0.05''$ for Jupiter's diameter of $42.1''$ at the time of observations corresponds to about 167 km . In the southern region the peak of the auroral emission lines is offset by 6 pixels ($\sim 1000 \text{ km}$) with respect to the peak of the CH_4 polar brightening (Kim et al., 1991) presumably due to the lower level $\text{H}_2\text{-H}_2$ collisional absorption (Kedziora-Chudczer & Bailey, 2011). In the northern region the corresponding offset is just 1 pixel from the brightened edge of the limb. The northern pole was oriented towards the observer at a distance of $20.6''$ from the centre of Jupiter's disc. In such a planetary orientation, taking into account the slit positioning in Figure 1, it is possible to see higher altitudes outside of the planetary limb in the southern polar region of the planet. The northern polar emissions can be visible above but mostly overlapping the northern edge of the limb in projection. Consequently the actual physical displacement of the aurora emissions from the brightened limb derived in previous modelling (Kim et al., 1992) and observations (Uno et al., 2014) translates more easily to our estimates for the southern region.

The extracted 1-D spectra were affected by absorption features due to strong telluric bands of CO_2 in parts of the K-band (regularly spaced dark lines in Figure 2). The usual procedure to deal with this contamination would be to divide our target spectrum by the spectrum of a telluric standard star that has been observed in temporal and spatial proximity to the target object. This would serve to remove any solar and telluric features resulting from the Earth's atmosphere. Here we applied a novel, more sophisticated and precise technique of telluric subtraction (Cotton et al., 2014) that is described in the next section. The extracted spectra of the northern and southern aurora were, in the first instance averaged over 4 pixels around the

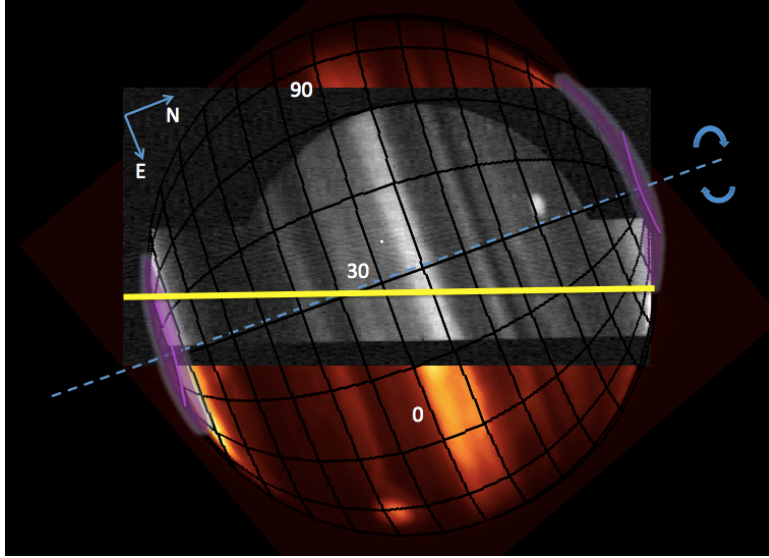


Figure 1: Acquisition image of Jupiter in the narrowband H_2 filter at $2.04 \mu\text{m}$ (in black-and-white) overlaid on the $2.1 \mu\text{m}$ image of the planet taken with the IRTF on July 19, 2009 (Credit: NASA/IRTF/JPL/University of Oxford). At the time of our observations the North pole was 20.6 arcsecond from the sub-observer point. The apparent longitude of the disk centre is about 31° in the λ_{III} coordinates system. The slit position is marked with the yellow line. The approximate extent of the UV auroral regions including the Io footprint, are plotted in purple, with purple lines denoting approximate position of the main ovals. The polar projections of these regions is shown in more detail in Figure 3.

peak emissions of H_3^+ . Due to non-symmetric positioning of the long slit and its smaller extent for the low-resolution settings, such spectra extracted from the northern regions are closer to the edge of the planetary limb. The most affected is the low-resolution spectrum of the northern aurora, where the emission features show only weakly against the stronger continuum from the disk of the planet.

3. ATMOF Telluric Model

The removal of the telluric absorption from our spectra was carried out using the ATMOF (ATMOspheric Fitting) code and related procedures (Cotton et al., 2014). This method was previously applied successfully to remove telluric lines from spectra of Jupiter and Titan, as well as Neptune (Cotton et al., 2015). A spectrum with telluric features that correspond to our

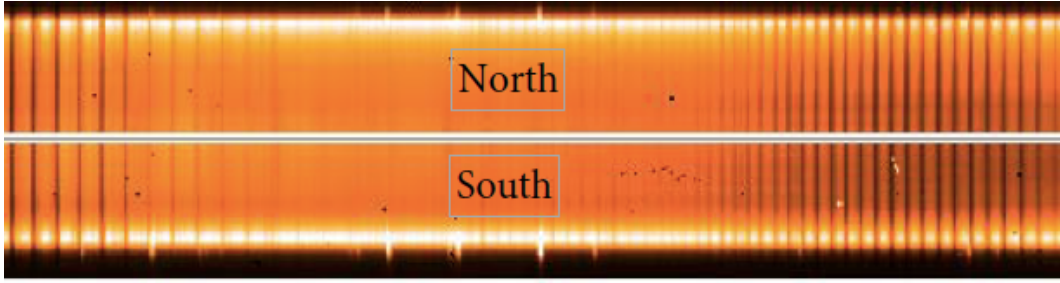


Figure 2: 2-D raw spectra of both polar regions across 60 pixels show auroral emissions at the edge of the planetary limb that are distinct from the brightening of the polar continuum in K band between 2.01 and 2.07 μm . Spectral resolution is $R \sim 18000$.

observations is derived by a modelling process, where a solar spectrum is passed through the Earth atmosphere model and the telescope instrumental response is subsequently applied. A number of free parameters such as CO_2 , H_2O content and the Doppler shift of the standard star are fitted to match the model spectrum to the standard star (HIP11503) data.

We used VSTAR - Versatile Software for the Transfer of Atmospheric Radiation (Bailey & Kedziora-Chudczer, 2012) to obtain the Earth atmosphere models for Mauna Kea Observatory with varied atmospheric content of carbon dioxide and water vapour. The CO_2 mixing ratio is varied as a fraction of the whole altitudinal profile, whilst the H_2O vapour mixing ratio is adjusted gradually only for the lower layers of the atmosphere as detailed in Cotton et al. (2014). In Figure 4(b) the model is shown that best matches telluric features present in the standard star. The telescope instrumental response consists of a scaling factor and slope, a wavelength shift correction, and the filter response for the GNIRS K-band order-blocking filter used in our observations, which is largely flat in the spectral region under consideration. In Figure 4(c) we show the solar spectrum as a composite of high-resolution data ($R = 300,000$) from the Kitt Peak Solar Atlas (Wallace et al., 1996), stitched together by using the low-resolution synthetic solar spectrum derived by Robert Kurucz¹ as a template for the intensity scale. At wavelengths below 2.02 μm the Kitt Peak data is incomplete, therefore

¹Kurucz, R. L. Accessed online on 12th January 2009. The solar irradiance by computation (<http://kurucz.harvard.edu/papers/irradiance/solarirr.tab>)

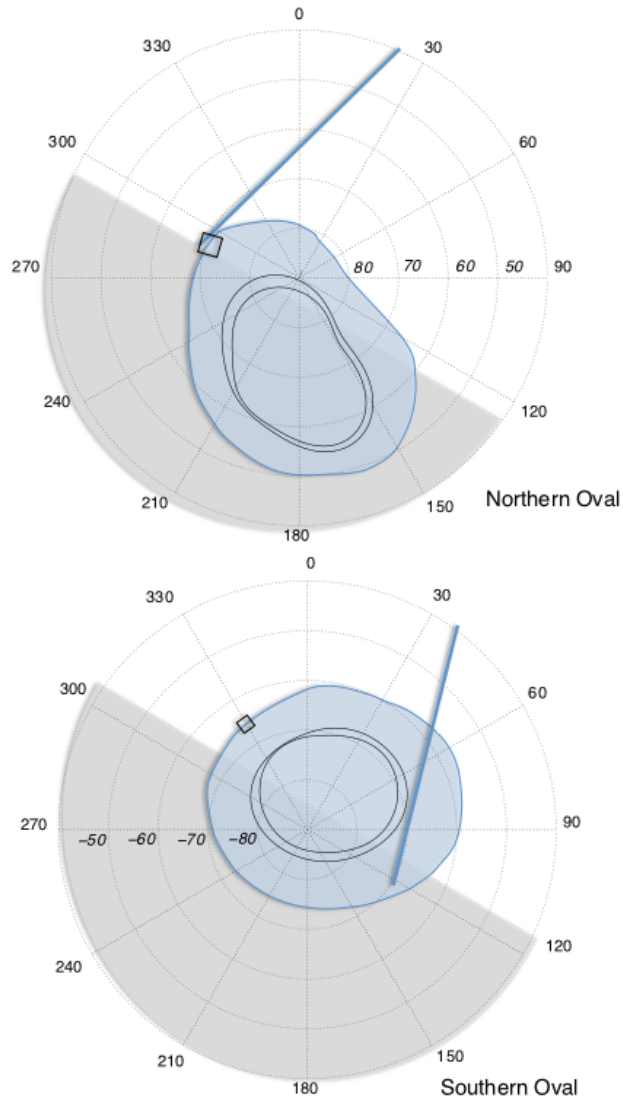


Figure 3: The northern and southern polar projections showing the extent of the typical UV aurora oval and Io footprint as defined in Grodent et al. (2003). The shaded regions define the night time during our observations. The slit position is approximated with the blue, straight lines. The black squares denote the expected position of Io footprint during our observations according to data from Bonfond et al. (2009).

the Kurucz’s low-resolution synthetic spectrum is substituted in this region (see Figure 1 in Cotton et al. (2014)).

Once the parameters for the Earth atmosphere model have been retrieved, the model is re-run with the zenith angle corresponding to the Jupiter observations. The Jovian auroral spectra are then divided by the telluric transmission, and the instrumental response with the retrieved parameters applied. This is followed by application of the wavelength shift to the Jovian auroral data, which is determined independently for each observation by fitting a Doppler-shifted solar spectrum passed through the Earth atmosphere model with telluric features. In this way the solar and telluric lines in the Jovian spectra can be used simultaneously to fine-tune the wavelength shift.

Finally we apply a baseline correction as a quadratic fit to the continuum that takes care of the residual background level remaining after sky subtraction due to unaccounted scattered light from the planet. The baseline subtracted varied slightly for all spectra, and was between 3 to 6.5% of the maximum signal intensity. This procedure is applied to all spectra extracted from the two-dimensional image shown in Figure 2 for the range of pixels where northern and southern auroral emission is visible. Also the 4-pixel-average of low and high-resolution spectra in Figure 5 and Figure 6 have been separately corrected with the ATMOF technique.

4. Identification of spectral lines in northern and southern regions

We used the Specview² tool for the analysis of 1-D spectra to fit Gaussian components to visible emission lines in order to derive their wavelengths and relative intensities. We fitted 26 emission lines in our high-resolution spectra. Additional emission features were fitted in the low-resolution datasets in spectral regions extending beyond the range of the high-resolution spectrum. Our detections of the H_3^+ transitions are listed in Table 2. In the high-resolution spectra we identified all the H_3^+ transitions expected in the region between 2.01 and 2.07 μm in temperatures $T_{rot} = T_{vib} = 1000$ K from the database in Neale et al. (1996). In the low-resolution spectra only some of the brightest transitions were clearly visible (see Comments in Table 2). The strongest H_3^+ transition visible in our low-resolution spectrum is tR(6,6) at 2.093 μm - outside the range of the high-resolution spectra.

²Specview can be found on the STScI website:
http://www.stsci.edu/institute/software_hardware/specview

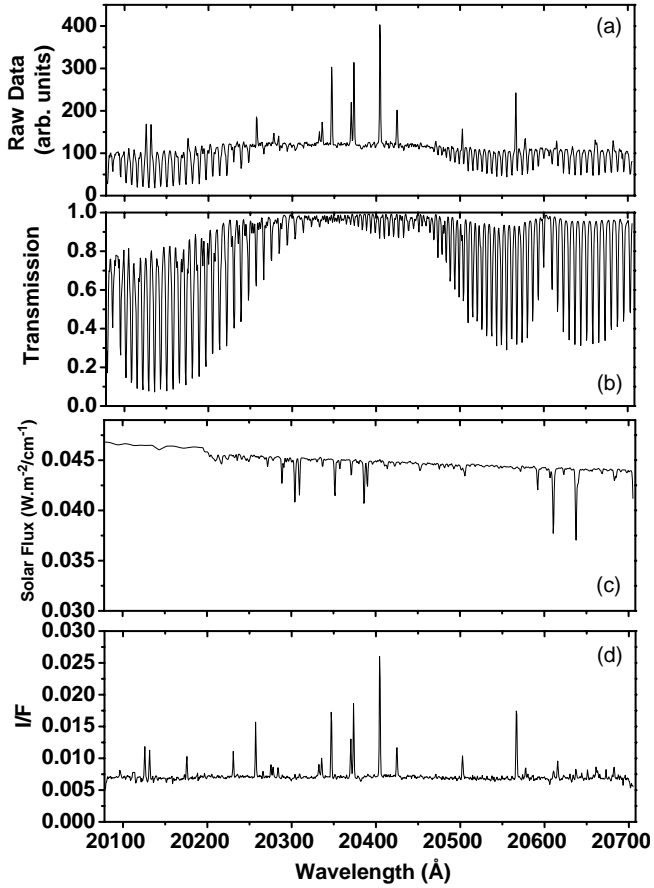


Figure 4: The spectral components used in the ATMOF modelling to remove telluric and solar features from the high-resolution spectrum of the southern auroral emission. (a) The 1-D spectrum of auroral emission before telluric subtraction, (b) The atmospheric model that provided best fit to the telluric features of CO_2 and H_2O absorption matching the standard star spectrum as applied to the Jovian spectra at the zenith angle of Jupiter's observations, (c) Solar spectrum described in Section 3, (d) Final 1-D spectrum after application of the ATMOF model.

In Figure 5 we marked the well known quadrupole transition from molecular hydrogen with H₂ 1-0 S(2) at 2.0338 μm in our high-resolution spectrum. In the low-resolution spectra for the southern region (Figure 6) the S(2) transition is also visible with the H₂ 1-0 S(1) and S(3) at 2.1218 and 1.9576 μm respectively. The corresponding H₂ transitions in the northern region are less pronounced, because the slit position did not extend beyond the planetary limb.

The fitted wavelengths of the H₃⁺ and H₂ lines in the high-resolution spectra show systematic shifts with respect to the vacuum wavelengths. The average difference between laboratory and observational assignments for the northern and southern aurora are 1.98 and 1.30 \AA respectively. The relative average wavelength difference in H₃⁺ and H₂ identifications between the two auroral regions of 0.68 \AA translates to 10.2 km/s difference in radial velocity, which can be explained by different and opposite Doppler shifts due to the rotation of the planet.

Beside the H₃⁺ and H₂ dominant transitions there are many more emission lines that we attempted to identify with different species that could be present in the Jovian aurora. We detect the atomic He I emission at 2.0587 μm in the high-resolution spectrum at low signal-to-noise level but with peak intensity that coincides with neither, H₃⁺ or H₂. Our high-resolution spectra contain many additional lines that have not been assigned before. Some of these features could be consistent with the low intensity transitions of H₃⁺, that are not present in the Neale et al. (1996) database. Uno et al. (2014) list additional transitions that coincide with lines visible in our spectrum such as P(5,4) at 2.0334 μm and P(5,3) at 1.9593 μm . It is not clear if the intensities of these additional assignments are consistent with the theoretical calculations (Lindsay & McCall, 2001).

We also considered the possibility that atomic transitions could be present in the spectral range under consideration. We used the NIST database (Kramida et al., 2015) to attempt matching any unassigned lines. Out of a large number of neutral and ionised atomic transitions expected in this spectral region, a significant fraction of them belongs to different excitation levels of Fe I; these were found to match closely many weaker lines observed in our spectra (Table 3).

We examined these assumed identifications and fitted the strongest lines with the Specview tool. Their wavelengths and relative intensities are given in Table 3 for spectra from Figure 5 and Figure 6. In Figure 7 we zoomed in on the faintest transitions in the high-resolution spectrum of the southern

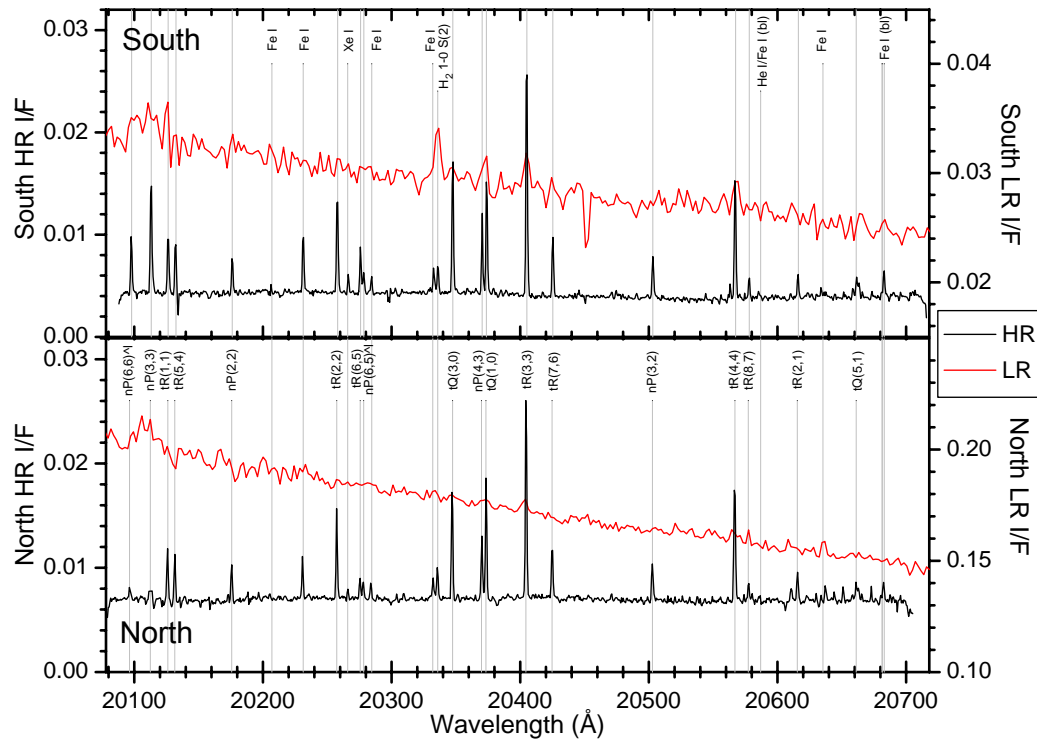


Figure 5: High-resolution (black) and over plotted low-resolution spectra in red for the southern (upper panel) and northern (bottom panel) aurora are shown. The radiance factor, I/F where I is the reflected intensity of the planet and πF is the solar flux incident on the planet, as defined in Kedziora-Chudczer & Bailey (2011). In the lower panel we marked the assignments of the H_3^+ transitions. In the upper panel the remaining identifications together with the proposed Fe I assignments are denoted.

aurora and marked the lines coinciding with the strongest Fe I lines expected in this region. The noise level in this spectrum is estimated to be 0.5×10^{-7} $\text{W m}^{-2} \text{sr}^{-1}$. In Table 3 we also list some of the strongest Fe I features that could possibly be detected in the low-resolution spectrum, especially for the southern auroral region, which extends further beyond the limb of the planet than the northern region. We suggest that a strong emission at $2.0268 \mu\text{m}$ (Figure 5) could be matched with the strongest Xe I transition expected in our observed region between 1.96 and $2.17 \mu\text{m}$. These possible assignments are discussed further in Section 9.4.

Table 2: The list of emission lines that were identified as H_3^+ transitions in spectra of both polar regions of Jupiter. All lines belong to $2\frac{1}{2} \rightarrow 0$ emission band. Fitted wavelengths and intensities are provided for all lines visible in the high-resolution spectra. Out of five additional transitions that are present in the low-resolution spectra, we were able to identify four of them in the southern auroral region and three in the northern region. In comments we note which transitions were visible in the low-resolution spectra, where (n) and (s) mean northern and southern aurora respectively.

Transition Wavenumber	Intensity ^a cm ⁻² atm ⁻¹	Vacuum wavelength Å	Branch & Transition	Southern Aurora		Northern Aurora		Comments
				Observed wavelength Å	Intensity ×10 ⁻⁷ Wm ⁻² sr ⁻¹	Observed wavelength Å	Intensity ×10 ⁻⁷ Wm ⁻² sr ⁻¹	
4732.041	5.238062	21132.53	tR(7,7)	21134.5	1.86	21101.4		low(n,s)
4777.226	13.509024	20932.65	tR(6,6)	20932.1	4.60	20925.2		low(n,s)
<i>High-resolution region starts</i>								
4839.508	1.645477	20663.26	tQ(5,1)	20663.45	5.86	20661.21	3.33	
4850.264	2.021775	20617.43	nP(2,1)	20616.26	3.00	20615.41	4.56	
4859.212	1.676679	20579.47	tR(8,7)	20578.04	2.40	20577.32	3.23	
4861.790	8.928174	20568.56	tR(4,4)	20567.43	14.93	20566.92	22.63	low(n,s)
4876.938	3.227214	20504.67	nP(3,2)	20503.10	4.82	20502.78	6.91	
4895.518	5.027651	20426.85	tR(7,6)	20425.37	6.77	20424.77	10.41	
4900.393	17.556369	20406.53	tR(3,3)	20405.19	27.27	20404.42	36.00	low(n,s)
4907.871	9.974512	20375.43	tQ(1,0)	20373.72	12.20	20373.34	18.93	low(s)
4908.672	6.496212	20372.11	nP(4,3)	20370.42	6.77	20369.91	10.72	
4914.248	11.810715	20348.99	tQ(3,0)	20347.58	14.29	20347.42	20.27	low(s)
4930.981	1.736462	20279.94	nP(6,5) ^l	20278.44	1.99	20278.31	3.01	
4931.596	3.475673	20277.41	tR(6,5)	20275.90	4.55	20275.61	3.71	
4936.000	7.481089	20259.32	tR(2,2)	20258.11	11.83	20257.39	14.39	
4955.991	4.101676	20177.60	nP(2,2)	20176.11	3.03	20175.70	5.71	
4966.838	4.391920	20133.53	tR(5,4)	20132.39	4.21	20131.44	7.26	
4968.272	5.010080	20127.72	tR(1,1)	20126.30	5.91	20126.04	8.15	low(s)
4971.561	10.582623	20114.41	nP(3,3)	20113.18	12.83	20112.45	14.44	low(n,s)
4975.338	4.023513	20099.14	nP(6,6) ^l	20097.93	4.93	20096.28	8.26	
<i>High-resolution region finishes</i>								
5000.499	9.807676	19998.00	tR(4,3)	19999.0	5.78	on CH ₄ absorption		low(s)
5032.447	4.824500	19871.05	tR(3,2)	19869.8	7.81	19870.0		low(n,s)
5094.218	8.831507	19630.10	tR(1,0)			severely affected by CH ₄ absorption		

^aThis is the integrated absorption intensity derived from the formula (3) in Neale et al. (1996) using the Online H₃⁺ Intensity Calculator from the H₃⁺ Resource Center (<http://h3plus.uiuc.edu/criteval/calc.shtml>) under assumption of T_{rot} = T_{vib} = 1000 K.

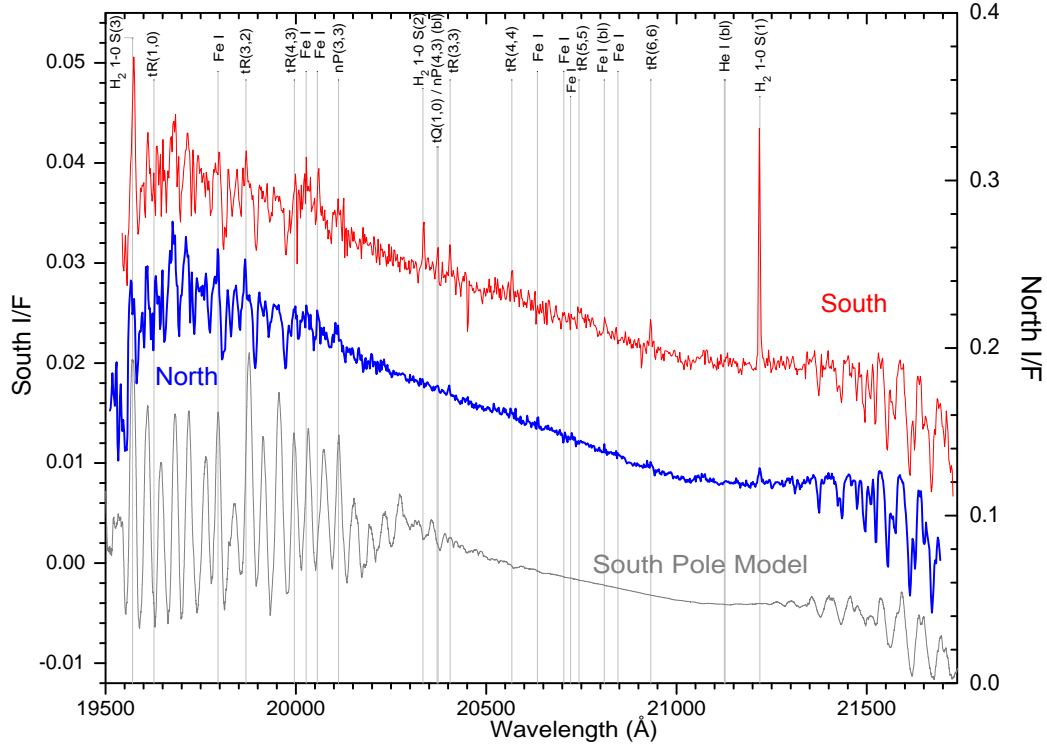


Figure 6: Low-resolution spectra for the southern (red) and northern (blue) aurora are presented. We also show a model of the atmosphere at the south polar limb of Jupiter, which was derived with the VSTAR modelling code. In the left and right ends of this spectral region there are strong bands of methane absorption in the atmosphere that make identification of only the strongest emissions possible when observed against the limb of the planet. We marked the positions of the lines expected in this part of the spectrum. The strongest lines belong to H_2 1-0 transitions. There are also strong H_3^+ transitions visible. We also marked positions of the strongest transitions of Fe I that should be visible in the low-resolution spectrum.

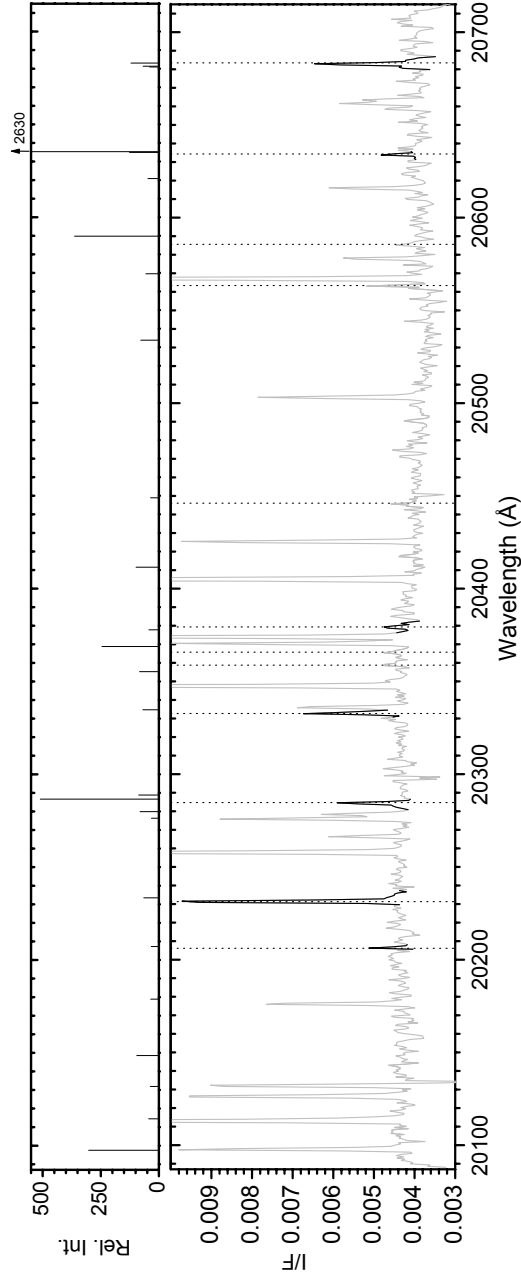


Figure 7: The Fe I transitions listed in column 2 of Table 3 are shown as a stick spectrum in the upper panel. Below we zoomed-in the high-resolution spectrum of the southern aurora to show the weak lines. It can be seen that the noise level increases only slightly at the edges of the spectrum due to removal of the strong CO₂ absorption bands. We marked the strong lines that we associated with the Fe I transitions in bold. The dotted lines are drawn to show the position of the closest unidentified lines observed near the listed Fe I transitions.

Table 3: The strongest Fe I transitions (above relative intensity 30) as listed in the NIST ASD database (Kramida et al., 2015) are reproduced in columns 2 and 3. The fitted corresponding wavelengths and intensities from the southern auroral region (unless indicated otherwise in Comments) are shown in column 4 and 5 respectively. These were derived predominantly from the high-resolution spectrum of the southern aurora. We show fits for only these lines that have a peak intensity above 1σ noise level estimated from the continuum between the strong lines. The low(n), low(s) and low(n,s) in Comments column denote possible detections in the low-resolution spectra either in northern, southern or both auroras respectively. For lines identified from the low-resolution spectra, only the wavelength of the peak emission is listed, because we found the intensity estimates difficult due to overlap with the strong methane absorption.

Transition cm ⁻¹	Observed Wavelength Å	NIST ASD Intensity ^a	Fitted Wavelength Å	Intensity ×10 ⁻⁷ W m ⁻² sr ⁻¹	Comments
5052.581202	19791.864	3160	19798.514		low(s)
4992.687211	20029.294	1480	20025.744		low(n,s)
4984.629397	20061.672	33	20060.391		low(n,s), inconsistent intensity, misidentification?
<i>High-resolution region starts</i>					
4975.732358	20097.544	302			overlap with nP(6,6) ^f
4971.542889	20114.48	44			overlap with nP(3,3)
4967.241045	20131.9	37			overlap with tR(5,4)
4963.134334	20148.558	95			possible feature within 1σ noise level
4955.666607	20178.92	35			overlap with nP(2,2)
4948.723309	20207.232	33	20206.111	1.09	
4942.298419	20283.501	65	20231.299	6.60	
4931.858971	20276.33	32			overlap with tQ(6,5)
4930.995404	20279.881	81			overlap with nP(6,5) ^f
4929.357379	20286.62	510	20284.676	1.99	
4928.814366	20288.855	87	(20289.693) ^b		marginal detection only in the northern spectrum
4917.691370	20384.745	69	20332.697	3.05	blends with H ₂ S(2) in low res. spectrum
4912.731225	20355.276	83	20358.754	0.59	
4909.462154	20368.83	245b1	20365.762	0.67	blends with nP(4,3) and tQ(1,0) in low res. spectrum
4907.298674	20377.81	43b1	20379.371	0.67	no clear detection
4899.185300	20411.557	98			no emission
4890.235007	20448.915	36b1	20446.095	0.76	overlap with tR(4,4)
4870.025354	20533.774	78			blend with He I at 20586.92Å line
4861.549393	20569.574	56	20563.438	2.05	no emission
4856.771384	20589.81	363b1	20585.602	0.98	blend with 20635.327Å line
4849.462970	20620.84	47			low(n)
4846.158223	20634.902	126	20634.322	1.43	blend with 20683.001Å line?
4846.058412	20635.327	2630			blend with 20683.001Å line
4835.373426	20680.926	40			
4835.276397	20681.341	68			
4834.888322	20683.001	120	20683.451	3.58	
<i>High-resolution region finishes</i>					
4829.993409	20703.962	600	20703.964		low(n,s)
4825.647428	20722.608	600	20722.597		low(n,s)
4806.465273	20805.310	500	20811.383		low(n,s) blend with 20810.774Å line
4805.203305	20810.774	690	20811.383		low(n,s) blend with 20805.310Å line

^aThe relative intensity as shown in the NIST ASD database Kramida et al. (2015), that use qualitative estimates taken from the sources referenced there.

^bThe wavelength estimate was derived from the peak in the northern spectrum.

5. Determination of average temperature and column density

Infrared auroral emission spectra of the H_3^+ have been used before to estimate the temperature of the upper thermosphere of the planet. Most of the early research was focused on the $\nu_2 \rightarrow 0$, fundamental emission spectrum at 3 to 4 μm that is much stronger than the $2\nu_2 \rightarrow 0$, overtone spectrum, with formally “forbidden” transitions (Drossart et al., 1989; Oka & Geballe, 1990; Lam et al., 1997; Miller et al., 1997). More recently observations of the H_3^+ , overtone spectra in selected regions of the K-band were investigated by independent groups (Raynaud et al., 2004; Uno et al., 2014). In 1999 and 2000 Raynaud et al. (2004) imaged the auroral emission of H_3^+ , calculated its rotational, vibrational temperatures (T_{rot} , T_{vib}) and column densities, $N(\text{H}_3^+)$ by using the high-resolution spectral region between 4700 and 4800 cm^{-1} (2.08 - 2.12 μm) with 13 overtone and 2 combination transitions.

In our analysis we compare two ways of deriving rotational temperature for our set of the H_3^+ identifications in averaged spectra at the peak emissions as defined previously (see Figure 5 and Figure 6). First we use the same method as Raynaud et al. (2004) under the assumption that emission regions are optically thin and local thermodynamic equilibrium (LTE) can be applied. We note that the ratios of all H_3^+ lines with respect to one specific line, can be fitted to obtain the T_{rot} by use of the following relationship:

$$T_{rot} = \frac{E'_i - E'_0}{k} \left[\ln \frac{g_i(2J'_i + 1)\nu_i A_i}{g_0(2J'_0 + 1)\nu_0 A_0} - \ln \frac{I_i(\nu_i)}{I_0(\nu_0)} \right]^{-1} \quad (1)$$

where J' is the rotational quantum number of the upper level, while E' is its corresponding energy. The ν is the transition frequency in cm^{-1} , A is the Einstein A coefficient for a given transition and k is the Boltzmann constant. The nuclear degeneracy factor, g is either 2, 4 or 8/3 (the modelling and assignment of these factors is explained further in Neale et al. (1996)). The zero subscript denotes the parameters for the reference transition, which was chosen to be nP(3,2) at 2.0504 μm . This line was reasonably strong and well separated from any neighbouring emissions that could affect its intensity. Here we make an important simplifying assumption that auroral regions can be described by the single kinetic temperature equal to rotational temperature derived from the H_3^+ emission ($T_{kin}=T_{rot}$).

To derive the fit for the temperature of both the northern and southern aurora regions, we used 16 lines from the high resolution averaged spectra of H_3^+ with the exception of the tQ(5,1) and tR(6,5) transitions, which have

significantly different intensities with respect to other lines in both spectra; they are clear outliers and blending with other nearby lines is a possible reason for inconsistencies in their intensity ratios. Our derived rotational temperatures, T_{rot} for northern and southern auroral region are 947 ± 43 K and 916 ± 58 K respectively.

In the second method for determining the rotational temperature, we simultaneously fit for rotational temperatures, T_{rot} , and column densities along the line of sight, $N(H_3^+)$. This is done with the assumption that, for optically thin emission in LTE, the column density of the H_3^+ emitting plasma is related to the intensity of lines and temperature as follows:

$$I_i(\nu_i) = \frac{N(H_3^+)g_i(2J'_i + 1)hc\nu_i A_i}{4\pi Q(T)} \exp \frac{-E'_i}{kT}, \quad (2)$$

where $Q(T)$ is a partition function at temperature T , while c is the speed of light. Specifically, this expression can be rewritten as

$$y = C - \frac{x}{T}, \quad (3)$$

with definitions

$$\begin{aligned} C &= \ln \left(\frac{N(H_3^+)}{Q(T)} \right), \\ x &= \frac{E'_i}{k}, \\ y &= \ln \left(\frac{4\pi I_i(\nu_i)}{g_i(2J'_i + 1)hc\nu_i A_i} \right). \end{aligned} \quad (4)$$

Accordingly, we numerically fit a line to the (x, y) coordinates via the standard Levenberg-Marquardt algorithm, as implemented in MATLAB. Confidence intervals for C and T can then be calculated using the inverse of Student's t cumulative distribution function. Consequently, the linear fits for both the northern and southern aurora regions are shown in Figure 8, as well as boundaries that account for a standard deviation in C and T values and boundaries that represent a 95% confidence interval for the fitting function.

From the slopes of these fits, we derive T_{rot} temperatures of 979 ± 49 K and 959 ± 61 K for the northern and southern auroral regions, respectively. These values are slightly higher than the temperatures obtained from the first method, but are in agreement within their uncertainties. Column densities

can then be derived from the y-intercepts, C , once T is known. So, for the northern aurora, possible densities range from 1.2×10^{16} to $7.0 \times 10^{16} \text{ m}^{-2}$ with the best estimate as $3.1 \times 10^{16} \text{ m}^{-2}$. Likewise, for the southern aurora, the best estimate is $5.2 \times 10^{16} \text{ m}^{-2}$, with one standard deviation in functional parameters resulting in a possible density range from 2.6×10^{16} to $8.1 \times 10^{16} \text{ m}^{-2}$. Although both methods are equivalent, using only relative line intensities in the first approach results in slightly reduced uncertainties on derived rotational temperatures. Given that auroral components sampled in the north and south are due to interaction of different parts of the magnetosphere with Jupiter’s ionosphere, the similar temperatures and column densities in both regions are noteworthy.

6. Vertical distribution of H_3^+ density profiles

We use the second method applied in Section 5 to obtain spatial profiles of temperatures and column densities for the spectra derived from the separate spatial pixels in the northern and southern auroral regions. Figure 9 shows the two-dimensional spectra in the regions under consideration and the corresponding intensity profiles, one across the brightest $2.0405 \text{ }\mu\text{m}$, H_3^+ line and the other across CH_4 , limb brightened continuum. The peak pixel in the $2.0405 \text{ }\mu\text{m}$ line profile is the same as peaks in all other H_3^+ identifications in our high-resolution spectra.

The fitted column densities, temperatures and spatial intensity profiles (Figure 10) show that the temperature remains relatively unchanged through all selected pixels where auroral emissions dominate, while the column density variation seems to correlate with the H_3^+ intensity profile. This was also noted in previously published observations by Lystrup et al. (2008). However they also observed a strong anticorrelation in temperature and column density. The higher column densities would be generated by the more energetic electrons penetrating deeper into the ionosphere where temperatures are lower. In our data we see only weaker such effects at high altitudes in the northern region, and in the southern auroral spectrum away from the limb towards the center of the planet, where there is also a hint of temperature decreasing. These differences, complicated by projection effects, could also be a result of increased noise in the regions overlapping the planetary limb and in the upper-most atmosphere due to low signal-to-noise. We intend to re-examine these trends in the new, currently scheduled observations.

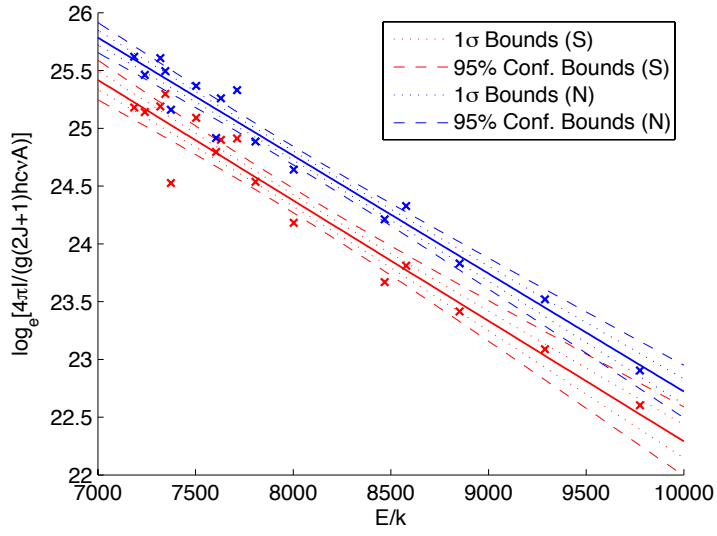


Figure 8: Lines of best fit for northern (blue) and southern (red) aurora data, according to Eq. (3). The functionals are bound by the dotted curves when one standard deviation of both C and T parameters is taken into account. They are also bound by the dashed curves with 95% confidence.

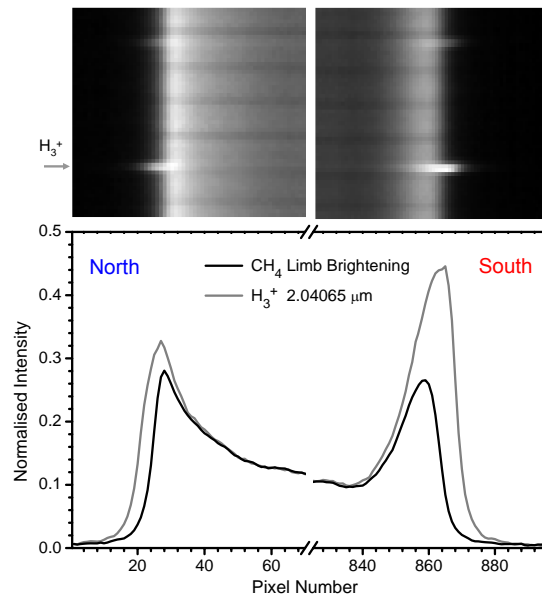


Figure 9: *Top:* Two dimensional spectra in the region around the $2.0405 \mu\text{m}$, H_3^+ line
Bottom: Intensity profiles corresponding to the H_3^+ line, and emission from the limb brightened continuum.

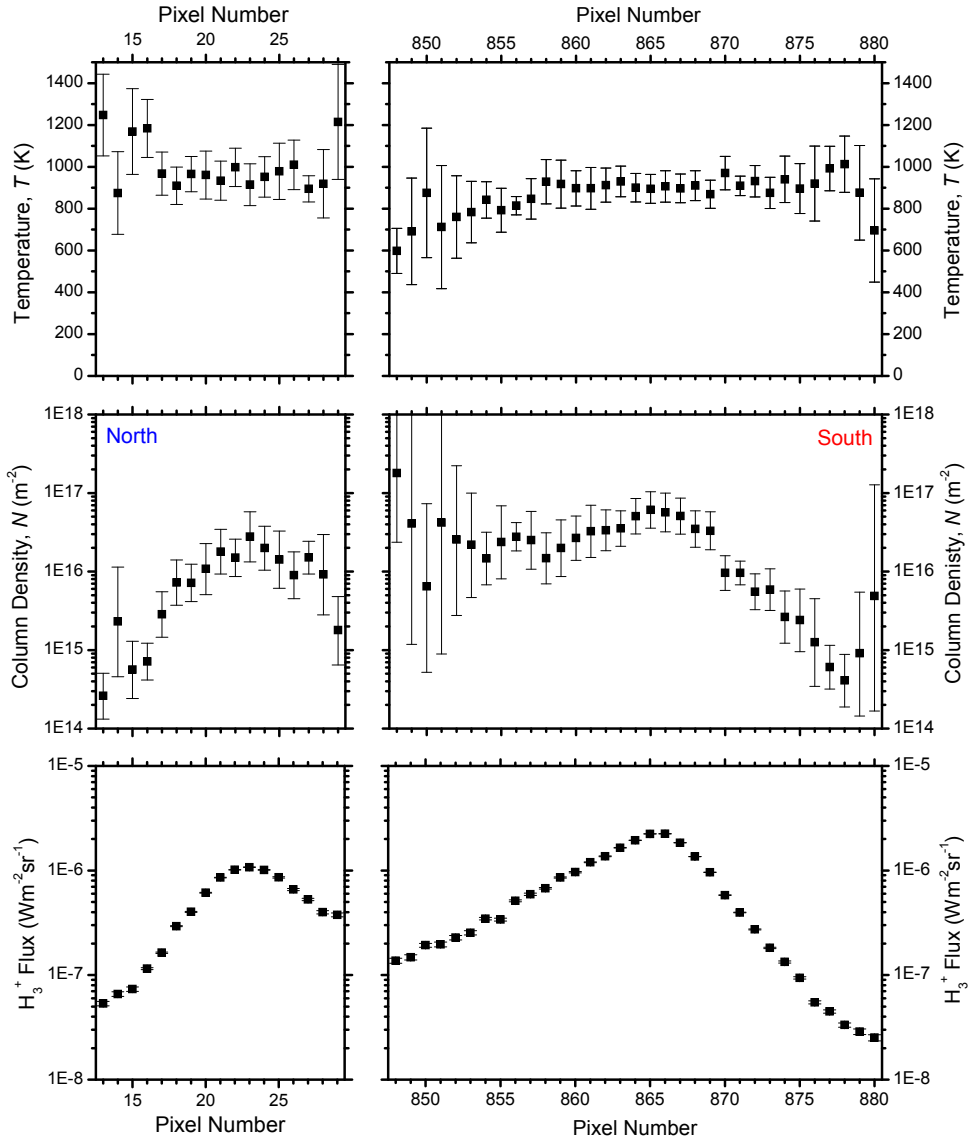


Figure 10: Temperature (*top*) and column density (*middle*) derived for spectra along single rows. H_3^+ intensity profiles (*bottom*) are shown for the brightest emission line for the northern and southern aurora.

Next we derive a vertical profile of ion density in both northern and southern aurora (Figure 11) by using the “onion peeling” technique, where we divided the region above Jupiter’s limb into concentric spheres of the size corresponding to the physical dimension of our pixels (see e.g. Uno et al. (2014); Lystrup et al. (2008)). This method allows taking account of a variation of column densities at different altitudes in the planetary atmosphere.

Figure 11 shows higher ion densities in the southern region, associated with the main oval emissions than ion densities observed in the Io footprint region in the north. However both profiles appear rather similar with the broad peak at 300 - 800 km above the limb brightening altitude. Similar analysis in Lystrup et al. (2008) leads to significantly higher derived peak ion densities and higher temperatures at the time of their observations in 2006 that reflects perhaps highly dynamic conditions in the ionosphere of the planet (see the review of previous measurements in Section 8). In common with Lystrup et al. (2008) our data also show temperatures outside of the limb relatively constant while the column densities keep decreasing. However we do not observe the decrease of temperature in the dusk part of the auroral region (our northern spectrum). This is most likely caused by the different orientation of our slit with respect to slit position in Lystrup et al. (2008), where we sample the emission along the auroral “curtain” in the vicinity of the Io spot, while they probe the region corresponding to the main oval in a direction perpendicular to the rotation axis.

7. H₂ quadrupole features in high and low-resolution spectra

In the spectral region explored in this study there are H₂ quadrupole $v=1$ to $v=0$ transitions that have been used in the past as probes of temperature and density of the emitting material (Kim et al., 1990). These transitions are thought to be excited due to either collisions or fluorescent emission. Our low-resolution spectrum of the southern auroral region shows a prominent emission feature from the 1-0 S(1) rotational-vibrational transition at 2.1218 μm . We can also clearly identify the 1-0 S(2) line at 2.0338 μm that is probably blended with the line at 2.0332 μm (that is visible in the high-resolution spectrum). At the low wavelength edge of this spectrum the strong line of 1-0 S(3) at 1.9576 μm can be seen (Figure 6). However it is difficult to define a continuum level around this line, which leads to large uncertainties in determining its intensity. The low-resolution spectrum of the northern region shows much weaker emission lines, which is not surprising as the slit did not

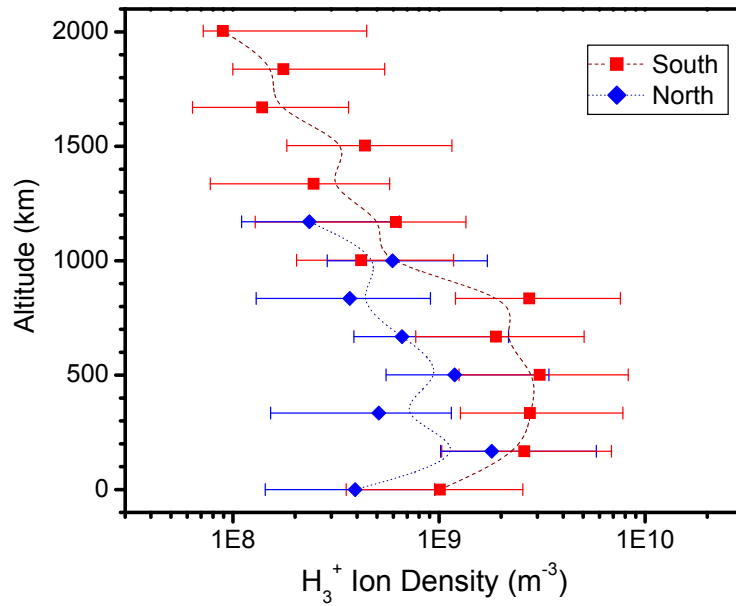


Figure 11: H_3^+ density profiles for the northern (blue) and southern (red) auroral regions. The spline fits to the profiles are shown with dotted lines. The errors were derived from the lower and upper bounds for column densities used in calculations.

extend beyond the limb of the planet and we do not see bright emission associated with the main Io spot but possibly a weaker arc of the footprint projected on the limb. Consequently both northern low and high-resolution spectra do not overlap spatially.

We used the spectrum for the southern aurora, where the H_2 lines are clearly detected to derive estimates of rotational temperature from the observed intensities of these three transitions. First we used Equation 1 and numerical values from Table 4 to solve for T_{rot} using 1-0 S(1) and S(2) lines that have well defined continuum levels. S(1) is an ortho and S(2) is a para state, therefore the assumptions about the ratio of both states has to be considered. At high temperatures in Jupiter’s ionosphere the H_2 para-ortho ratio can be reasonably assumed to be 0.25. Using this ratio we calculated the rotation temperature, $T_{rot} = 575 \pm 245$ K, where the errors were derived from the estimate of 1 sigma deviation from the flux measurement of each line.

We repeated this procedure for the 1-0 S(1) and S(3) lines with the advantage of using both transitions in the same, ortho state. However as we noted before the S(3) line is placed in the region of the residual absorption of the CH_4 band, and it is impossible to derive precise level of continuum for this line. The 1-sigma error bar on the flux estimate of this line is affected by its systematic component rather than a statistical deviation. The resulting temperature derived from the use of these two transitions was $T_{rot} = 1025 \pm 350$ K, which is consistent with the temperature for 1-0 S(1) and S(2) transitions within the range of the largest uncertainties derived in both cases. If we use higher values of the para-ortho ratio, this leads to lower temperature estimates from the 1-0 S(1) and S(2) pair. Kim et al. (1990) suggest that a ratio of 0.273 is a reasonable limit for the regions of the lower stratosphere where the in-situ measurements made with the Voyager’s IRIS spectrometer (Kim et al., 1985) indicate temperatures of 170 K, and the auroral H_2 longitudinal position varies on time-scales that are much shorter than possible for the ortho-para ratio to reach equilibrium.

Table 4: Observed quadrupole H₂ transitions in low-resolution spectra. The intensities are provided for the southern auroral region. J' is the rotational quantum number for the upper state, g_n is the statistical weight of the nuclear spin, which depends on the spin alignment of both nuclei in H₂. At high temperatures g_n of para states is 1 and ortho states is 3.

Transition	Laboratory wavenumber cm ⁻¹	Vacuum wavelength Å	Observed wavelength Å	J'	g_n	Upper Energy Level ^a K	Einstein Coeff. A_{ij} s ⁻¹ × 10 ⁻⁷	Measured Intensity W m ⁻² sr ⁻¹
1-0 S(1)	4712.905	21218	21217	3	3	6956	3.47	3.5±0.2×10 ⁻⁶
1-0 S(2)	4917.007	20338	20335	4	1	7584	3.98	6.1±1.0×10 ⁻⁷
1-0 S(3)	5094.218	19576	19574	5	3	8365	4.21	1.9±0.6×10 ⁻⁶

^aThe upper energy level is based on online data provided by D. L. DePoy where the rotational term value for upper state is derived by using constants from Dabrowski (1984).

8. Previous measurements of temperatures and column densities of H_3^+ in auroral regions

8.1. Temperatures

After the discovery of the near infrared $2\nu_2$ overtone band of H_3^+ from Jupiter's aurora (Trafton et al., 1989; Drossart et al., 1989), the focus of subsequent observations quickly moved to the fundamental emissions that occur at $3.5 \mu\text{m}$. These are of an order of magnitude brighter and placed against the background of the dark limb of the planet. The estimates of H_3^+ effective temperatures were derived using both fundamental and overtone bands showing rotational temperature values in the vicinity of 1000 K.

The rotational temperature derived by Drossart et al. (1989) from the first identified lines in the overtone band was close to 1100 K under the assumption of LTE. In 1990 the first measurement of the H_3^+ temperature from the fundamental band with the UKIRT telescope gave a significantly lower value of 670 K (Oka & Geballe, 1990). Interestingly the overtone band at $2 \mu\text{m}$ was not detected during that time, which implied, perhaps not surprisingly given observations of our Earth auroral emissions, that auroral emissions can vary in time. Miller et al. (1990) were able to detect both bands on the same night and found their relative intensities indicated that H_3^+ vibrational levels 1 and 2 are populated as expected at the vibrational and rotational temperature of 1100 ± 100 K in thermal equilibrium. This also suggested that the dominant process in H_3^+ is collisional excitation by H_2 and He rather than the resonant vibrational exchange with H_2 . Kim et al. (1992) tested the assertion about the H_3^+ emissions arising in thermal equilibrium. They calculated the vibrational distribution of the molecule over the range of altitudes in the ionosphere assuming electron influx below levels needed to produce the UV aurora. They concluded that at the peak of H_3^+ emissions the radiation losses are almost the same as collisional losses, which would lead to slight overpopulation of lower vibrational levels compared with the Boltzmann distribution.

Observations of the vertical and spatial distribution in auroral H_3^+ emission suggest that it peaks at around $0.2 \mu\text{bar}$, which is equivalent to an altitude of 650 km above the cloud deck. Maillard et al. (1990) showed significant differences in rotational temperatures between northern (830 ± 50 K) and southern (1000 ± 40 K) auroral regions at $4 \mu\text{m}$. Subsequent imaging with narrow band filters showed that the auroral emission was clearly localised in "hot spots" (Baron et al., 1992). Miller et al. (1991) used a $2.7''$ beam placed

on the limb of Jupiter and confirmed significant differences between northern and southern temperatures of H_3^+ emission. In addition, the temperature of the northern aurora appeared to drop by 200 K within one day.

Later, more detailed mapping with higher spatial resolution revealed arc-like structures of strong emission surrounded by a diffuse, low intensity area (Sato et al., 1992). In fact Miller et al. (1997) find that H_3^+ emission persists at all latitudes within a few percent of auroral intensity. A spectroscopic study by Lam et al. (1997) at 3.47 and 4.00 μm allowed mapping of the H_3^+ temperature and column density distribution over the entire disk of Jupiter with a resolution of about 10° in latitude. Maxima of temperatures are observed in the polar regions and are close to 1000 K. The highest estimate of H_3^+ auroral temperatures came from the work of Stallard et al. (2002) who measured the “hot band” transition $\text{R}(3,4^+)$ at 3.94895 μm together with the fundamental band $\text{Q}(1,0^-)$ line throughout the regions of auroral emission, allowing derivation of vibrational temperature, which ranged from 900 to 1150 K. Similarly high temperatures were derived by Drossart et al. (1993) from the estimates of Doppler widths in observed lines from the collisional broadening.

We noted in Section 5 the imaging of auroral zones using overtone band H_3^+ emission lines by Raynaud et al. (2004) led to estimates of both rotational and vibrational temperatures due to the presence of lines from the overtone and hot bands in the spectral region examined. The average T_{rot} of the $v_2 = 2$ level was determined to be 1170 ± 75 K while $T_{vib} = 960 \pm 50$ K for the $v_2 = 3$ level. Again such a difference suggests that the higher level $v_2 = 3$ is underpopulated as compared to expectation from the LTE. The rotational temperatures derived from our spectra in Section 5 are slightly below 1000 K for both northern and southern auroras and are broadly consistent with the range of values derived from the past observations of the overtone band.

8.2. Column density

Even before the discovery of H_3^+ emission in Jupiter’s ionosphere, its column density was predicted from theoretical models that assumed production of H_3^+ by ionisation of H_2 and its destruction due to recombination with electrons. McConnell & Majeed (1987) estimated the maximum concentration of H_3^+ above 1000 km above the cloud deck and its column density between 6 and $10 \times 10^{16} \text{ m}^{-2}$.

The first measurements of column density from observations of the $2\nu_2 \rightarrow 0$ band at 2 μm gave a value three orders of magnitude lower than theoretical

estimates, $2.8 \times 10^{13} \text{ m}^{-2}$ (Drossart et al., 1989)³. Maillard et al. (1990) estimated column density from $\nu_2 \rightarrow 0$ band observations under the assumption of thermal equilibrium and also found it lower than theoretical predictions. They measured $3.3 \times 10^{14} \text{ m}^{-2}$ in the southern auroral region. In two observations three days apart they obtained 1.2 and $2.4 \times 10^{14} \text{ m}^{-2}$ in the northern auroral region.

In a model of vibrational distribution of H_3^+ , Kim et al. (1992) find its peak to be slightly higher than 650 km above the cloud deck and derive maximum column densities at the peak to be consistent with the observations. In addition, their model shows column densities of the overtone band systematically lower than the fundamental band as a function of height. This also appears to be supported by previously published observations. Since their model suggested a deviation from local thermal equilibrium at the peak of H_3^+ , any measurements that assumed LTE should be treated as lower limits to actual levels of its column density.

Notably the first measurements of column densities were averages over several thousands of kilometres of Jupiter’s area, because the spectra were obtained with low spatial resolution. Observations of the full planetary disk at 3.47 and 4.0 μm with close to 10^4 km resolution show a significant column density of H_3^+ at above $0.1 \times 10^{16} \text{ m}^{-2}$ that is also measured at the equatorial latitudes (Lam et al., 1997). The subsequent mapping observations (Stallard et al., 2002; Raynaud et al., 2004) revealed the rather complex and time variable distribution of H_3^+ within auroral regions. Stallard et al. (2002) who scanned the northern auroral region in two emission lines of H_3^+ over five nights, find significant variation in average column density in the range from 0.58 to $1.1 \times 10^{16} \text{ m}^{-2}$. The most detailed maps of column density in both northern and southern auroral regions were derived in ($2\nu_2 \rightarrow 0$) $2 \mu\text{m}$ band with the extreme values close to 10^{19} m^{-2} in the arc-like feature of the northern aurora.

Our measurements of $N(\text{H}_3^+)$ with $3.1 \times 10^{16} \text{ m}^{-2}$ and $5.1 \times 10^{16} \text{ m}^{-2}$ for the northern and southern auroras respectively, are consistent with previous observations that had comparable spatial resolution to what can be achieved with the Gemini telescope.

³The original value of column density for $2\nu_2 \rightarrow 0$ band was corrected in Maillard et al. (1990).

9. Discussion

Our detections of auroral emission lines and subsequent measurements of rotational temperature, T_{rot} and column density of the H_3^+ emissions are just one spatial and temporal snapshot that shows only one aspect of the energy exchange processes in Jupiter’s ionosphere.

Dedicated observations of auroral emission in infrared bands with 8-m class telescopes like Gemini and larger are still quite rare despite the clear advantage of superb spatial resolution of the Jovian disk achievable from the ground. Two recently published studies show such results of observations taken with the largest telescopes. The Keck II telescope mapping of emissions in L-band (Lystrup et al., 2008) with NIRSPEC and observations with the IRCS spectrometer on the Subaru telescope in K-band (Uno et al., 2014) allowed derivation of vertical ion density and emissivity profiles based on echelle spectra of H_3^+ taken with resolution better than the $R = 18000$ observations reported here.

9.1. Spectroscopy of auroral emissions

Long slit observations provide typically better throughput and less chance of spurious lines from overlapping orders as compared with multi-dispersing designs. This is particularly useful for examining the low intensity features seen in our spectra, obtained with the highest resolution of GNIRS. The infrared windows in K and L bands, where the methane absorbs almost completely any thermal emission from the planet, are naturally chosen for observation of auroral emission.

However telluric absorption due to molecules in the Earth’s atmosphere requires very careful calibration that is often too difficult using the traditional method of subtracting a spectrum of the standard star from the target object. In addition, the standard star’s spectral type has to be closely matched to solar G2V to avoid stellar lines imprinting on the target spectrum. This method can leave spurious residual features in spectra, as seen for example in Figure 4 of Uno et al. (2014), where telluric absorption of CO_2 bands around 2.0 and 2.06 μm in Figure 4(b) were overcorrected. The intensity of spurious emission lines in their spectra is sometimes higher than the weak lines assigned to H_3^+ , which can lead to misidentifications. The ATMOF method (Cotton et al., 2014) used for our spectral calibration deals more precisely with the effects of telluric absorption. This allows us to study any weak emissions, such as lines visible in “zoomed in” Figure 7.

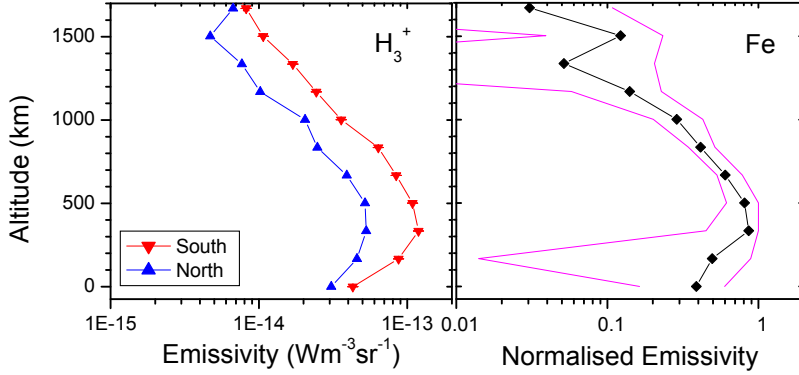


Figure 12: *Left:* Emissivity profiles of the H_3^+ 2.0405 μm line for the southern and northern auroral region. *Right:* The average normalised emissivity profile of two strongest lines Fe I 2.0234 and 2.0284 μm combined for both regions. The upper and lower bounds shown in the figure represent the highest and lowest normalised emissivities amongst the four lines.

9.2. The H_3^+ spatial distribution and correlation with H_2 emission

Our resulting rotational temperatures and column densities of H_3^+ for the small portions of Jupiter aurora covered by the GNIRS spectra are similar to the values derived for well spatially resolved maps of auroral emissions (Lam et al., 1997; Raynaud et al., 2004). A single position of the slit provides very limited information on the vertical distribution of the peak of H_3^+ emission. The vertical emissivity profile for H_3^+ was derived by application of the “onion peeling” technique for the northern and southern regions (Figure 12). The peak of emissivity is visible within the broad layer centered at 400 km above the peak of the limb brightening discussed previously, which is defined as the zero altitude. We attempted to obtain vertical emissivity profile for H_2 from the line at 2.0334 μm as well. It suggests a more uniform emissivity distribution over the region of altitudes covered in Figure 12. The difference is reasonably well visible in the intensity profiles of H_2 and H_3^+ emission along the slit for both auroral regions (Figure 13), which is not surprising considering the chemistry of both molecules.

The formation mechanism of H_3^+ involves collisions of H_2 with ionised molecular hydrogen. The produced ion is vibrationally excited and this energy is re-radiated in infrared spectral lines such as presented in this report. This radiative cooling is an important process in energy balance of the ionosphere, together with radiative cooling by CH_4 and C_2H_2 at the lower atmospheric heights. In the upper ionosphere the H_3^+ ion is destroyed by interaction with an electron in dissociative recombination, a mechanism that adds heat into the ionosphere. The lifetime of the ion depends on the density of electrons which seem to peak at low altitudes (below 1000 km) during dusk, and at 1500 to 2000 km at dawn (Yelle and Miller, 2004). The corresponding lifetimes of H_3^+ ion are of the order of 10 to 100 sec. In the Jovian aurora the main source of electrons available to ionise hydrogen is the solar wind (Baron et al., 1992) and the ions formed from gases emitted by volcanic activity on Io that are trapped in the planetary magnetic field and spiral down towards its surface along field lines. Our emissivity profiles for H_3^+ ion in the northern and southern regions that correspond to dusk and dawn limbs respectively, show peaks at significantly different altitudes, which may be related to different electron densities in these regions. Another reason for this difference could be the geometry of the emissions in both regions. In the south the slit covers more of the auroral oval and our line of sight cuts through longer extents of brighter emission, while in the north we do not sample emission associated with the main auroral oval but a slightly weaker emission from the Io footprint. The statistical altitude of the peak UV emission for the main Io spot was suggested to be 900 ± 125 km from the 1 bar level (Bonfond et al., 2009), which is significantly higher than our peak of the volume emissivity at ~ 650 km for H_3^+ (assuming the limb brightening position at 200 km above 1 bar level). This difference could be explained by our observations corresponding to higher energies of precipitating electrons than suggested in Bonfond et al. (2009).

The quadrupole transitions of H_2 in K-band were associated with Jupiter's aurora before discovery of the overtone H_3^+ in that region (Trafton et al., 1989). There is still some debate over the similarity in spatial distribution of both molecules. Although spatially resolved ultraviolet observations with the HST (Gerard et al., 1993) were first to note very close correspondence of H_2 to H_3^+ emissions, the maps in Raynaud et al. (2004) seem to show significant differences in the relative intensity of emission for both molecules. Proposed reasons for this could be a variable ortho-to-para ratio in H_2 distribution or dynamic changes due to supersonic winds (Stallard et al., 2001; Rego et al.,

1999) Considering vertical distribution of H_2 and H_3^+ , the model by Kim et al. (1992) suggests the peak intensity of their emission at the same height, close to 600 km above the cloud deck. This conclusion was supported by observations of emissivity profiles undertaken by Uno et al. (2014). Our emissivity profile derived from only one weak line of H_2 is not sufficiently reliable to reach firm conclusions about the altitude differences between both species. However the distribution of intensities along the slit in Figure 13 suggests the H_2 emission peaks slightly below the H_3^+ , and the emissivity is reduced less rapidly with increasing altitude compared with the H_3^+ ions.

9.3. The LTE considerations

Temperatures derived from infrared emission lines of H_3^+ are associated with the transitions present in the observed portions of its ro-vibrational spectrum. Our data allows only determination of the rotational temperature, because only transitions from the single $2\nu_2 \rightarrow 0$ overtone band are identified in the spectral region between 2.01 and 2.07 μm . A comparison of line intensities for two different vibrational bands is required to assess whether T_{rot} is also a thermal temperature of H_3^+ in the ionosphere, which means that the relative populations at different vibrational levels follow a Boltzmann distribution (are in thermal equilibrium).

In a previous study Miller et al. (1990) measured the vibrational temperature from line intensities of both fundamental and overtone bands and found it consistent with the rotational temperatures, which suggests that H_3^+ is in the LTE condition. In addition the translational temperatures measured from resolved line shapes and compared with rotational temperatures (Drossart et al., 1993) suggest that T_{rot} represents the kinetic temperature in Jupiter’s ionosphere. However this assertion is not entirely correct since models (Kim et al., 1992; Melin et al., 2005) show that at the altitude of the strongest H_3^+ emissions the rate of radiative cooling and collisional de-excitations becomes similar for the $2\nu_2$ and ν_2 vibrational levels. Although the ratio of populations at these levels satisfies the Boltzmann distribution, the ground level is excessively populated by radiative cooling. This effect becomes even more important at higher altitudes and it affects cooling efficiency of H_3^+ in the upper ionosphere.

Grodent et al. (2001) developed a two-stream electron transport model which links the spectrum of incident electrons with distribution of vertical temperature in the ionosphere. Since H_3^+ thermal emissions are affected

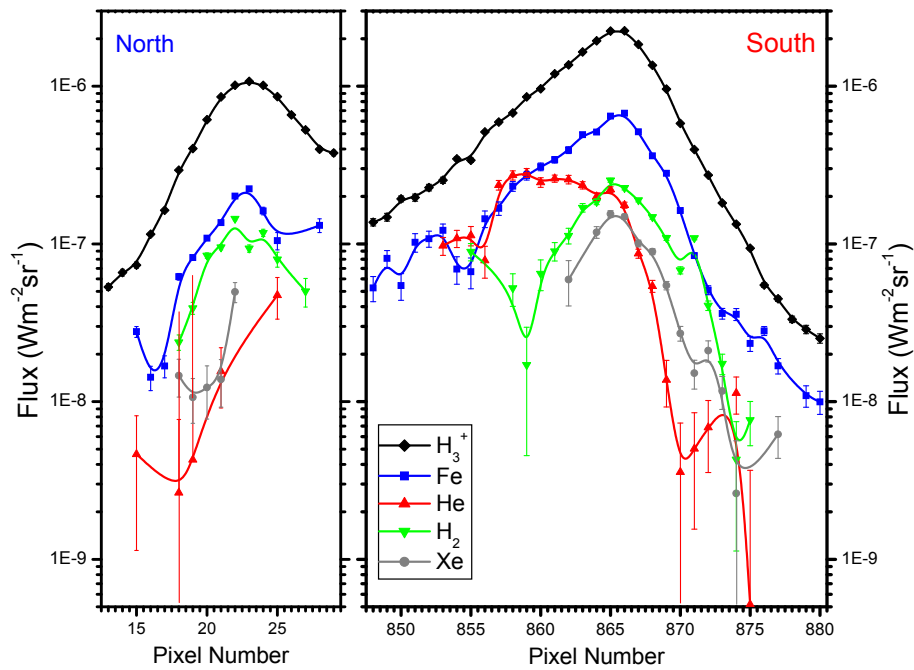


Figure 13: Intensity profiles of the emission lines that belong to assigned atomic and molecular species. $\text{H}_3^+ - 2.0405 \mu\text{m}$, $\text{Fe I} - 2.0231 \mu\text{m}$, $\text{Xe I} - 2.0268 \mu\text{m}$, $\text{H}_2 - 2.0338 \mu\text{m}$ and $\text{He I} - 2.0587 \mu\text{m}$ are shown in the plots. The lines connecting data are the spline fits to the profiles.

mainly by the soft-energy electrons (3 keV), they conclude that they cannot be used to derive the entire energy driving the auroral display. Thermal emissions from H_2 and C_2H_2 should be used to help constrain the high-energy end of the electron flux component. Uno et al. (2014) modeled the altitude profiles for one of the H_3^+ lines from $2\nu_2$ vibrational levels under assumption of the LTE and used a broader distribution of electron fluxes than assumed in Grodent et al. (2001). The resulting emissions peaked at altitudes above 1000 km – much higher than the 400–800 km suggested by their observations. Similarly our data suggest lower peak altitudes around 600 km. Uno et al. (2014) showed that relaxing the LTE assumption could bring the peak altitudes in closer agreement with their estimates from observations (Figure 11).

Mapping observations (Raynaud et al., 2004; Stallard et al., 2002) suggest a clear spatial correlation of emission line intensity with column densities of H_3^+ and only marginal correlation with temperatures. In Figure 10 temperature profiles fitted to our data across the slit are relatively constant while column densities are correlated with H_3^+ emission distribution. Since H_3^+ acts like a very efficient thermostat the increase in temperature leads to a faster cooling rate, which in turn moderates overall changes in temperature. Therefore observed line intensities are more representative of column densities in the upper ionosphere and are most sensitive to the H_3^+ distribution. It is important to note that depending on the amount of deviation from LTE conditions the fitted temperatures underestimate the actual temperature and the ion density derived from the column density, $N(\text{H}_3^+)$ (Melin et al., 2005).

9.4. Additional emission lines in high-resolution spectra.

Figure 5 shows that all H_3^+ lines, which have transitions in the $2\nu_2 \rightarrow 0$ overtone band in this spectral region, were easily identified. However these spectra show a few more emission lines, most of them weak but also a few relatively strong that do not correspond to any confirmed transitions of H_3^+ (Neale et al., 1996). Beside the expected H_2 quadrupole S(2) line at $2.0334 \mu\text{m}$ and the resonant He I at $2.0587 \mu\text{m}$, there are strong features at 2.0231 , 2.0284 , 2.0289 , 2.0332 , 2.0635 and $2.0683 \mu\text{m}$ that were missing identification. We examined the high-resolution spectra for potential sources of spurious lines and hypothesised that some of these emissions could be due to atomic species and searched the NIST database (Kramida et al., 2015) for appropriate identifications.

Voyager 1 *in situ* observations of Jupiter’s magnetosphere detected a torus-shaped cloud of heavy ions and energetic neutral atoms (mainly oxygen, sodium and sulfur) that originate from the volcanic activity of Io (Krimigis et al., 2002; Mendillo et al., 2004). At first a precipitation of these ions into high latitudes along magnetic field lines was thought to provide enough energy to excite Jupiter’s aurora (Gehrels & Stone, 1983); this idea was subsequently disputed by Gladstone et al. (2002). Ionised atoms are typically observed by their X-ray emissions (Elsner et al., 2005). Recent observations of Jovian transmission spectrum by Montanes-Rodriguez (2015) reveal the presence of neutral sodium in the upper atmosphere of the planet. They suggest its origin from either cometary impacts, as observed during the collision of comet Shoemaker-Levy 9 (SL9) in 1994 (Noll et al., 1995), or due to deposition from Io into a toroidal area around the planet.

There are 377 different atomic transitions listed in the NIST database within the range of our high-resolution spectrum. We examined lines from different atomic species by use of their relative intensities (keeping in mind that these are rather uncertain parameters). If the strongest transitions of a given (neutral or ionised) atom were clearly not visible in our spectrum, this would make this species an unlikely identification, even if some lines matched its weaker transitions. We found the most consistent matches with Fe I transitions and also identified a strongest emission of Xe I in this region. Finding matches with Fe perhaps should not be surprising, since its abundance is high in the interstellar medium. Iron also has a complex and rich energetic structure. In our spectral region Fe I has close to a third of all transitions listed. Although this could be a reason why we are more likely to match our lines with the Fe transitions, the transitions of ionised iron are almost twice as common as Fe I, so we would expect them to match lines in our spectra more often than transition for neutral iron if the matches were random. In such a case we would also expect matches with many other atomic species. There is no strong correlation between the intensities listed in the database and those observed in our spectrum, which is a result of either incorrect assignments or the very different conditions under which the lines listed in the database were observed compared with the conditions of Jupiter’s atmosphere.

Figure 7 shows a zoomed-in spectrum in order to focus on weaker lines. The upper panel shows the stick spectrum of Fe I transitions, which are aligned with our high-resolution spectrum. We marked lines in black when there is a good match with transitions listed in Table 3 in bold. The dotted lines are centred on the peaks of the lines that are the closest to known Fe I

transitions, the weakest of them are clearly just above our signal-to-noise level. In Table 3 we comment on the possible problems with the individual assignments.

In Figure 13 we plotted the intensity profiles of lines of different species including our Fe I assignments. All of them are similar in shape to H_3^+ profile with a notable exception of the resonant He I line with a broader intensity peak that appears much closer to the limb of the planet. Of course a possible reason for the similarity of H_3^+ and Fe I profiles could be incorrect assignment of unknown H_3^+ transitions. However such unknown transitions are likely to be considerably weaker than observed unassigned lines in our spectrum.

In the right panel of Figure 12 we show the averaged emissivity profile for the Fe I identifications obtained with the onion peeling method. Initially we plotted the strongest two Fe lines from each hemisphere, and discerned no significant differences in their emissivity-altitude profiles. Subsequently the data for these lines (2.0234 and 2.0283 μm) for northern and southern regions have been merged as follows. For each line the data is normalised to the altitude of greatest emissivity. The average of the four normalised lines at each altitude has then been plotted in Figure 12. The upper and lower bounds shown in the figure represent the highest and lowest normalised emissivities amongst the four lines. The normalised Fe emissivity has been plotted over the same number of decades as the corresponding H_3^+ emissivity in the left panel of the figure for easy comparison of their rates of change. Profiles for both species appear to have the strongest emissivity at similar altitude.

The only published observations of iron emissions in Jupiter’s atmosphere were the HST/FOS UV spectrum taken after the impact of the SL9 comet (Figure 4 in Noll et al. (1995)) and the spectrum of optical emission from two multiplets at 0.445 and 0.52 μm centred on the comet impact sites (Fitzsimmons et al., 1996). Solar fluorescence was suggested as a mechanism of the UV emissions rather than a collisional excitation that is less efficient in higher levels of Jupiter’s atmosphere, however optical emissions were assumed to arise due to thermal excitation of the cometary material.

Neutral iron emission due to fluorescence was observed in the Earth air-glow during twilight at 0.3860 μm by Tepley et al. (1981). A possible source of Fe I at the heights close to 100 km in the Earth’s atmosphere is suggested to be meteor ablation. Similar processes could lead to periodic occurrence of neutral and ionised iron in the high levels of Jupiter’s atmosphere. The infrared emission of neutral Fe I is produced by transitions at high excitation states. Such highly excited atoms are thought to originate from a recomb-

nation of Fe ion (Nave et al., 1994), which could be important in the auroral regions of Jupiter with the enhanced electron density.

Grebowky (1981) and later Kim et al. (2001) derived a model of the ion densities for the products of meteoric ablation in Jupiter’s atmosphere. They find a layer of ions that peaks at the altitudes of around 400 km above the level of 1 bar pressure. This peak is dominated by the contribution of Mg II and Fe II with the ion density close to 10^{10} m^{-3} . The total density of ions remains similar at the higher levels of the ionosphere but it is dominated by the H_3^+ contribution, while the Fe II ion density drops steadily to negligible value at altitudes close to 1000 km. Grebowky (1981) estimated production rate of the neutral Fe at the higher altitudes to be orders of magnitude larger than Fe II. The emissivity of neutral Fe I from the lines detected in our spectra in Figure 12 peaks around 600 km above 1 bar pressure, which is higher than suggested by the model for ionised content of the ionosphere. In future investigations we intend to model the characteristic de-excitation times for these possible Fe I transitions, which will help us to derive their density profiles and compare them with estimates for the ionised Fe II distribution.

10. Conclusions

In summary, we obtained high- and low-resolution spectra of Jupiter’s two auroral regions with GNIRS on the Gemini North telescope. The northern region is likely to be associated with the main spot in the Io footprint and the southern region samples the area of the main oval. We identified strong emission lines from the H_3^+ overtone band and H_2 quadrupole emissions in both low- and high-resolution spectra. We also tentatively suggested assignment of weaker lines with atomic transitions of Fe I, He I and Xe I. Our use of ATMOF fitting allowed a superior removal of telluric absorption from CO_2 bands. This improves our confidence in fitting and assigning weaker lines in the spectra.

Transitions of H_3^+ were used to derive rotational temperature and column density for both northern and southern auroral regions, and we found that our values are broadly consistent with previously published measurements. We derived vertical emissivity and H_3^+ ion density profiles of both auroral regions which includes an estimate of the altitude for the emission peak associated with the main oval of the Io footprint. Since we were not able to determine if the rotational temperature derived here is a true kinetic temperature due to observations of only one vibrational band of H_3^+ and we also had very limited

spatial information about observed emissions, we intend to make additional long slit auroral mapping observations with the GNIRS at L and K band almost simultaneously to constrain the parameters derived from H_3^+ . These observations are planned during the Juno mission flight over polar regions in order to measure electron density distribution together with associated UV and infrared emissions.

New spectra obtained in the spatial mapping mode will also help us to determine the identifications and provide emissivity profiles of lines that have not yet been assigned. Our spectra will extend over a wider range of wavelengths that will allow us to search for the stronger lines of neutral or ionised atomic ions and to confirm or disprove our tentative observations of neutral iron lines. This extended spectral coverage will also allow us to understand the spatial distribution of the weak He I emission.

Although Jovian aurora have been studied by different methods that provided clues about origin, physical conditions, heating/cooling processes, energy transport and LTE balance; many results are still debated. Monitoring of auroral emissions is even more important at the time when the Juno mission is starting to release the first data for *in situ* study of Jupiter's upper atmosphere, magnetosphere and auroras. Continuation of ground-based studies is intended to place Juno's observations in a global context. Jupiter's auroral emission provides a laboratory from which we can draw analogies for possible observations of such emissions in the exoplanets, brown dwarfs and late type stars like the recently observed aurora detected in the M8.5 dwarf, LSR J1835+3259 (Hallinan et al., 2015).

Acknowledgments

This work is based on observations (GN-2011B-Q-1) obtained at the Gemini Observatory, which is operated by the Association of Universities for Research in Astronomy, Inc., under a cooperative agreement with the NSF on behalf of the Gemini partnership: the National Science Foundation (United States), the National Research Council (Canada), CONICYT (Chile), the Australian Research Council (Australia), Ministério da Ciência, Tecnologia e Inovação (Brazil) and Ministerio de Ciencia, Tecnología e Innovación Productiva (Argentina). We also wish to thank Professor Michael Burton for his helpful discussion and advice that benefitted this paper. We wish to thank the anonymous referees for the follow-up research suggestions that helped us to improve the paper.

References

References

- Adamowicz L., Pavanello M., 2012, Progress in calculating the potential energy surface of H_3^+ , *Phil. Trans. R. Soc. A.*, 370, 5001–5013
- Bailey J., Kedziora-Chudczer L., 2012, Modelling the Spectra of Planets, Brown Dwarfs and Stars using VSTAR, *MNRAS*, 419, 1913–1929
- Baron R. J., Owen T., Tennyson J., Miller S., Ballester G. E., 1992, Imaging Jupiter’s aurorae in the 3 to 4 micron band of H_3^+ , *Nature*, 353, 539–542
- Bhardwaj A., Gladstone G. R., 2000, Auroral emissions of the giant planets, *Reviews of Geophysics*, 38, 295–353
- Bonfond, B., Grodent, D., Gerard, J.-C., Radioti, A., Dols, V., Delamere, P. A. and Clarke, J. T., 2009, The Io UV footprint: Location, inter-stop distances and tail vertical extent, *J. Geophys. Res.*, 114, A07224, doi:10.1029/2009JA014312
- Bonfond B., Hess S., Bagenal F., Garard J.-C., Grodent D., Radioti A., Gustin J., Clarke J. T., 2013, The multiple spots of the Ganymede auroral footprint, *Geophysical Research Letters*, 40, 4977–4981
- Cotton D. V., Kedziora-Chudczer L. L., Bott K., Bailey J., 2015, Atmospheric Modelling for Neptune’s Methane D/H Ratio - Preliminary Results, *Proc. 14th Australian Space Research Conference*. Adelaide ISBN 13: 978-0-9775740-8-7, p.13–24
- Cotton D. V., Bailey J., Kedziora-Chudczer L., 2014, Atmospheric modelling for the removal of telluric features from infrared planetary spectra, *MNRAS*, 439, 387–399
- Dabrowski I., 1984, The Lyman and Werner bands of H_2 , *Canad. J. Phys.*, 62, 1639–1664
- Drossart P., Maillard J.-P., Caldwell J. et al., 1989, Detection of H_3^+ on Jupiter, *Nature*, 340, 539–541
- Drossart P., Maillard J.-P., Caldwell J., Rosenqvist J., 1993, Line-resolved spectroscopy of the Jovian H_3^+ auroral emission at 3.5 micrometers, *ApJ*, 402, L25–L28

- Elsner R.F, Ramseya B.D., Waite Jr. J.H., Rehak P., Johnson R. E., Cooper J. F., Swartz D. A, 2005, X-ray probes of magnetospheric interactions with Jupiter's auroral zones, the Galilean satellites, and the Io plasma torus, *Icarus* 178, 417–428
- Fitzsimmons A., Andrews P. J., Catchpole R., Little J. E., Walton N., Williams I. P, 1996, Reentry and Ablation of the Cometary Dust in the Impact Plumes of Shoemaker-Levy-9, *Nature*, 379, 801–804
- Gerard J C., Dols V., Paresce F., Prange R.. 1993, Morphology and time variation of the Jovian far UV aurora: Hubble Space Telescope observation, *J. Geophys. Res. Planets* 98, 18793–18801
- Gehrels N., Stone E. C., 1983, Energetic oxygen and sulfur ions in the Jovian magnetosphere and their contribution to the auroral excitation, *J. Geophys. Res.* 88, 5537–5550
- Gladstone G. R., Waite J. H., Grodent D., Lewis W. S., Crary F.J., Elsner R. F., Weisskopf M. C., Majeed T., Jahn J.-M, Bhardwaj A., Clarke J. T., Young D. T., Dougherty M. K., Espinosa S. A., Cravens T. E., 2002, A pulsating auroral X-ray hot spot on Jupiter, *Nature*, 415,1000–1003
- Grebowsky J. M., 1981, Meteoric ion production near Jupiter, *J. Geophys. Res.*, 86, 1537–1543
- Grodent D., Waite J. H., Gerard J. C., 2001, A self-consistent model of the jovian auroral thermal structure, *J. Geophys. Res.*, 106, 12933–12952
- Grodent D., Clarke J. T., Kim, J., Waite Jr, J. H., Cowley W. H., 2003, Jupiter's main auroral oval observed with HST-STIS, *J. Geophys. Res.*, 108, 1389–1403
- Hallinan G., Littlefair D. P., Cotter G., Bourke, S., Hardinget L.K. et al. 2015, Magnetospherically driven optical and radio aurorae at the end of the stellar main sequence, *Nature*, 523, 568–571
- Kedziora-Chudczer L., Bailey J., 2011, Modelling the near-infrared spectra of Jupiter using line-by-line methods, *MNRAS*, 414, 1483–1492
- Kedziora-Chudczer L., Bailey J., Horner J. 2013, Observations of the D/H ratio in Methane in the atmosphere of Saturns moon, Titan - where did the

- Saturnian system form?, Proc. of the Australian Space Science Conference 2012, ISBN 13: 978-0-9775740-6-3 p.53–64
- Kim S. J., Cadwell J., Rivolo A. R. Wagener R., Orton G. S., 1985, Infrared polar brightening on Jupiter, 3, Spectrometry from the Voyager 1 IRIS experiment, *Icarus*, 64, 233–248
- Kim S. J., Drossart P., Caldwell J., Maillard J.-P., 1990, Temperatures of the Jovian auroral zone inferred from $2\mu\text{m}$ H_2 quadrupole line emission, *Icarus*, 84, 54–61
- Kim S. J., Drossart P., Caldwell J., Maillard J.-P., Goorvitch, D. Moorwood, A., Moneti, A. and Lecacheux, J., 1991, The $2\mu\text{m}$ polar haze of Jupiter, *Icarus*, 91, 145–153
- Kim Y. H., Fox J. L., Porter H. S., 1992, Densities and vibrational distribution of H_3^+ in the Jovian auroral ionosphere, *J. Geophys. Res.*, 97, 6093–6101
- Kim S. J., Pesnell W. D., Grebowsky, J. M. and Fox, J. L. 2001, Meteoric Ions in the Ionosphere of Jupiter, *Icarus*, 150, 261–278
- Kramida A., Ralchenko Y., Reader J. and NIST ASD Team, 2015, NIST Atomic Spectra Database (ver. 5.2), [Online]. Available: <http://physics.nist.gov/asd> [2015, February 7]. National Institute of Standards and Technology, Gaithersburg, MD.
- Krimigis S. M., Mitchell D.G., Hamilton D.C. Dandouras, J, Armstrong, T. P., Bolton, S. J., Cheng, A. F., Gloeckler, G., Hsieh, K. C., Keath, E. P., et al., 2002, A nebula of gases from Io surrounding Jupiter, *Nature*, 415, 994–996
- Lam H.A., Achilleos N., Miller S., Tennyson J., Trafton L. M., Geballe T. R., Ballester G. E., 1997, A baseline spectroscopic study of the infrared auroras of Jupiter, *Icarus*, 127, 379–393
- Lindsay C. M., McCall B.J., 2001, Comprehensive Evaluation and Compilation of H_3^+ Spectroscopy, *J. Mol. Spectroscopy*, 210, 60–83
- Lystrup M. B., Miller S., Dello Russo N., Vervack Jr. R. J., Stallard T., 2008, First Vertical Ion Density Profile in Jupiter’s Auroral Atmosphere: Direct Observations Using the Keck II Telescope, *ApJ*, 677, 790–797

- Maillard J.-P., Drossart P., Wattson J. K. G., Kim S. J., Caldwell J., 1990, H_3^+ fundamental band in Jupiter's auroral zones at high-resolution from 2400 to 2900 inverse centimeters, *ApJ*, 363, L37–L41
- McConnell J. C., Majeed T., 1987, H_3^+ in the Jovian ionosphere, *J. Geophys. Res.*, 92, 8570–8578
- Melin H., Miller S., Stallard T., Grodent D., 2005, Non-LTE effects on H_3^+ emission in the jovian upper atmosphere, *Icarus*, 178, 97–103
- Mendillo M., Wilson J., Spencer J., Stansburry J. 2004, Io's volcanic control of Jupiter's extended neutral clouds, *Icarus*, 170, 430–442
- Miller S., Joseph R. D., Tennyson J., 1990, Infrared emissions of H_3^+ in the atmosphere of Jupiter in the 2.1 and 4.0 micron region, *ApJ*, 360, L55–L58
- Miller S., Lam H. A., Tennyson J., Ridgway S., Joseph R. D., 1991, Spectroscopy of H_3^+ in the Jovian Atmosphere, *Bull. Am. Astron. Soc.*, 23, 1136
- Miller S., Achilleos, N., Ballester, G. E. Lam H. A., Tennyson J., Geballe T. R., Trafton, L. M., 1997, Mid-to-Low Latitude H_3^+ Emission from Jupiter, *Icarus*, 130, 57–67
- Montanes-Rodriguez P., Gonzalez-Merino B., Palle E., Lopez-Puertas, M., Garcia-Melendo, E., 2015, Jupiter as an exoplanet: UV to NIR transmission spectrum reveals hazes, a Na layer, and possibly stratospheric H_2O -ice clouds, *ApJL*, 801, L8–L13
- Nave G., Johansson S., Learner R. C. M., Thorne A. P., Brault J. W., 1994, A new multiplet table for Fe I, *ApJS*, 94, 221–459
- Neale L., Miller S., Tennyson J., 1996, Spectroscopic Properties of the H_3^+ Molecule: A New Calculated Line List, *ApJ*, 464, 516–520
- Noll K. S., McGrath M. A., Trafton L. M., Atreya S. K., Caldwell J. J., Weaver H. A., Yelle R. V., Barnett, C. Edgington S., 1995, HST Spectroscopic Observations of Jupiter After the Collision of Comet Shoemaker-Levy 9, *Science*, 267, 1307–1313
- Oka T., Geballe T. R. 1990, Observations of the 4 micron fundamental band of H_3^+ in Jupiter, *ApJ*, 351, L53–L56

- Oka T., 1992, The infrared spectrum of H_3^+ in laboratory and space plasmas, *Rev. Mod. Phys.*, 64, 1141–1149
- Raynaud E., Lellouch E., Maillard J.-P., Gladstone G. R., Waite J. H., Bozard B., Drossart P., Fouchet T., 2004, Spectro-imaging observations of Jupiter’s 2-m auroral emission. I. H_3^+ distribution and temperature, *Icarus*, 171, 133–152
- Rego D., Achilleos N., Stallard T., Miller S., Prange R., Dougherty M., Joseph R. D., 1999, Supersonic winds in Jupiter’s aurorae, *Nature*, 399, 121–124
- Satoh T., Connerney J. E. P., Baron, R., 1996, Emission Source Model of Jupiter’s H_3^+ Aurorae: A Generalized Inverse Analysis of Images, *Icarus*, 122, 1–23
- Stallard T., Miller S., Millward G., Joseph R. D., 2001, On the Dynamics of the Jovian Ionosphere and Thermosphere. I. The Measurement of Ion Winds, *Icarus*, 154, 475–491
- Stallard T., Miller S., Joseph R. D., Millward G., 2002, On the Dynamics of the Jovian Ionosphere and Thermosphere. II. The Measurement of H_3^+ Vibrational Temperature, Column Density, and Total Emission, *Icarus*, 156, 498–514
- Tepley C. A., Meriwether Jr J. W., Walker J. C. G., Mathews J. D., 1981, Observations of neutral iron emission in twilight spectra, *J. Geophys. Res.*, 86, 4831–4835
- Thompson J. J., 1911, Rays of Positive Electricity, *Phil., Mag.*, 21, 225–249
- Thorne R. M., Tsurutani B. T., 1979, Diffuse Jovian aurora influenced by plasma injection from Io, *Geophys. Res. Letters*, Vol. 6, 649–652
- Trafton L., Lester D. F., Thompson, K. L, 1989, Unidentified emission lines in Jupiter’s northern and southern 2 micron aurorae, *ApJ*, 343, L73–L76
- Uno H. A., Kasaba Y., Tao C., Sakanoi T., Kagitani M., Fujisawa S., Kita H., Badman S. V., 2014, Vertical emissivity profiles of Jupiter’s northern H_3^+ and H_2 infrared auroras observed by Subaru/IRCS, *J. Geophys. Res. Space Physics*, 119, 10219–10241

- Wallace L., Livingston W., Hinkle K., Bernath P., 1996, Infrared Spectral Atlases of the Sun from NOAO, *ApJ*, 106, 165–169
- Yelle R.V., Miller, S., 2004, Jupiter's Thermosphere and Ionosphere, "The planet, Sattelites and Magnetosphere" ed. F. Bagenal, T.E. Dowling and W. B. McKinnon, 185–218